

Discovery of anomalous nuclear effect on electron transfer between atoms

Sota Kimura^{a,*}, Michiharu Wada^a, Hiromitsu Haba^b, Hironobu Ishiyama^b,
Toshitaka Niwase^c, Marco Rosenbusch^b, Peter Schury^a

^a *Wako Nuclear Science Center (WNSC), Institute of Particle and Nuclear Studies (IPNS), High Energy Accelerator Research Organization (KEK), Wako, Saitama, 351-0198, Japan*

^b *RIKEN Nishina Center for Accelerator-Based Science, Wako, Saitama, 351-0198, Japan*

^c *Department of Physics, Kyushu University, Fukuoka, Fukuoka, 819-0395, Japan*

* Corresponding author. Email: sota.kimura@kek.jp

Abstract

Among the known isotope effects in chemistry, electron spin conversion by nuclear spin is a potent mechanism governing the reactions of radical pairs. For the electron transfer between nonradical(s), this spin conversion does not work, and other isotope effects have been presumed to have negligible contributions. However, we have observed a nuclear-state-dependence anomaly in ion charge state distributions in the thermalization of energetic atomic ions in helium gas, the process between nonradical(s). It could be understood to arise from the change in the stability of the intermediate quasi-molecule state of the electron transfer caused by the difference in nuclear states. This should prompt a reconsideration of the influence of atomic nuclei on interatomic and intermolecular interactions.

The difference in chemical properties among different isotopes of a chemical element is known as isotope shift. The isotope shift originates from two properties of atomic nuclei: the effect of differences in the isotopic masses is known as the mass-dependent isotope effect (MDE) and is described by the framework of Bigeleisen-Myer theory [1], while the size and shape of atomic nuclei result in the nuclear field shift effect (NFSE) [2], which is categorized as the mass-independent isotope effect (MIE).

Interest in the effect of nuclear spin on the chemical reactions of “radicals,” which are atoms and molecules having unpaired valence electrons, has existed since at least the 1970s [3]. This effect is known as the magnetic isotope effect, based on the spin conversion of the radical pairs via the interactions with nuclear spin. This is one of the MIEs and is a more potent mechanism for controlling the chemical reactions compared with the NFSE. Recently, its role in the biochemical processes has been focused [4].

On the other hand, nuclear spin changes the levels of atomic states through the hyperfine interaction. The magnitude of energy shift in atomic states due to hyperfine splitting is $\sim 10^{-5}$ eV; therefore, the influence of nuclear spin on the electron transfer (ET) between atoms had been presumed negligible. However, we have discovered an anomaly

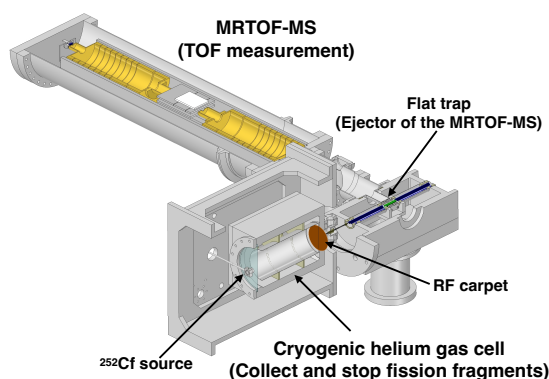


Figure 1: Schematic view of the experimental setup. Adopted from [6] with modification.

in the ion charge state distribution (ICSD) resulting from the ETs between helium atoms and radioactive isotope ions having various nuclear states, the reactions with nonradical-radical and nonradical-nonradical pairs.

Fission sources constantly provide various atomic nuclei (including their isomeric states) at a steady intensity. By employing a multi-reflection time-of-flight mass spectrograph (MRTOF-MS) [5], their relative ratios can be determined accurately under identical conditions. This capability is what enabled the present discovery.

Figure 1 illustrates the experimental setup [6]. The various radioactive ions produced via spontaneous fission of a 9.25-MBq ^{252}Cf source (fission branch: 3.09%) were collected by a cryogenic helium gas cell (CHeGC). When the incoming ions pass through a thin Mylar window sealing the CHeGC, their charge states are expected to be around or larger than $q = 15+$ (hereafter, a specific charge state is denoted as $n+$). They lost their charges via the ETs with the filling helium gas, and their mean charge state was around $2+$ when thermalized in the CHeGC. The stopped ions were extracted by a radio-frequency carpet [7] without contacting the component parts of the CHeGC and then were transported to a flat trap, the injector for the MRTOF-MS. After that, their time-of-flight (TOF) spectra were measured with the MRTOF-MS. The CHeGC was cryogenically cooled throughout the measurements, and the filling helium gas was provided from helium cylinders of purity > 99.99995 vol% and purified with a three-stage purification system consisting of two getters (SAES MonoTorr and MicroTorr) and a cold trap having a temperature below 10 K to suppress other noble gasses. This purification system facilitates the removal of contaminants to achieve an extremely clean environment.

Figure 2 shows a set of TOF spectra focusing on the mass number (A) = 97 isobar series as an example of the fission fragment measurements with the MRTOF-MS. Both atomic and molecular ions can be found in the TOF spectrum. The intensity ratios of the

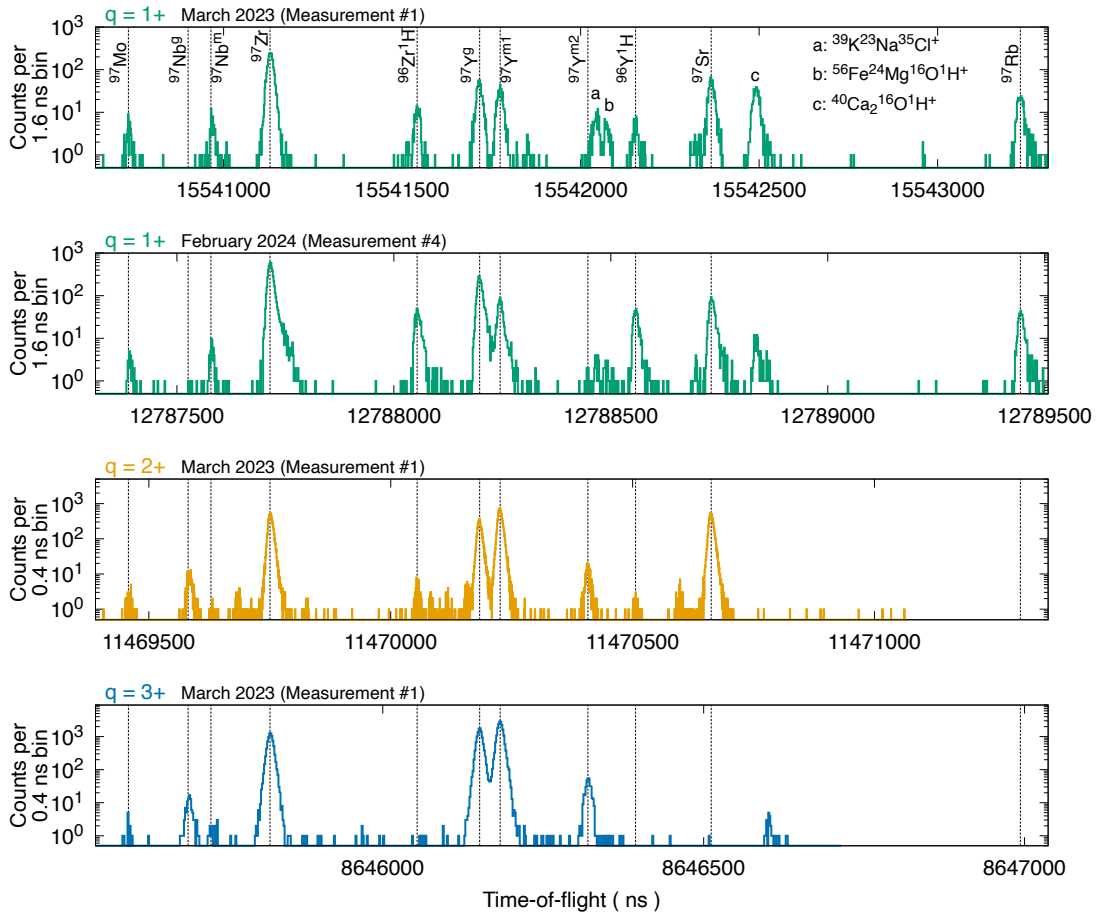


Figure 2: Time-of-flight spectra focusing on $A = 97$ isobar series. The vertical dotted lines show the predicted position of each ion species. The unlabeled peaks in $q=1+$ TOF spectra are the molecules of stable isotopes. For $q = 1+$, the results of the measurements at two different periods are shown.

observed ions are not constant across charge states due to differences in the chemical properties of elements; for example, the peak of ^{97}Rb can be found in the spectrum of $1+$ but is not observed in that of $2+$.

As the MDE and the MIE vary negligibly between nuclear ground and isomeric states when considering the ETs with the nonradical, neutral helium atoms, the isomeric yield ratios for any given nuclide should naively be conserved with respect to the charge state. However, in our measurements, we find otherwise. Consider ^{97}Nb and ^{97}Y , as shown in Fig. 2, where the isomeric yield ratios vary considerably between $1+$ and $2+$. Given this fact, the isomeric yield ratio measurements were carried out for several nuclides across the $1+$, $2+$, and $3+$. Figure 3 shows the observed TOF spectra for the various isomer-exhibiting nuclides studied; the horizontal axis has been converted to the mass-energy relative to the ground state of each nuclide. Contrary to expectation, the relative intensities of the isomeric states relative to the ground state were not constant with respect to the charge state. Then, to investigate whether this phenomenon is universal, we

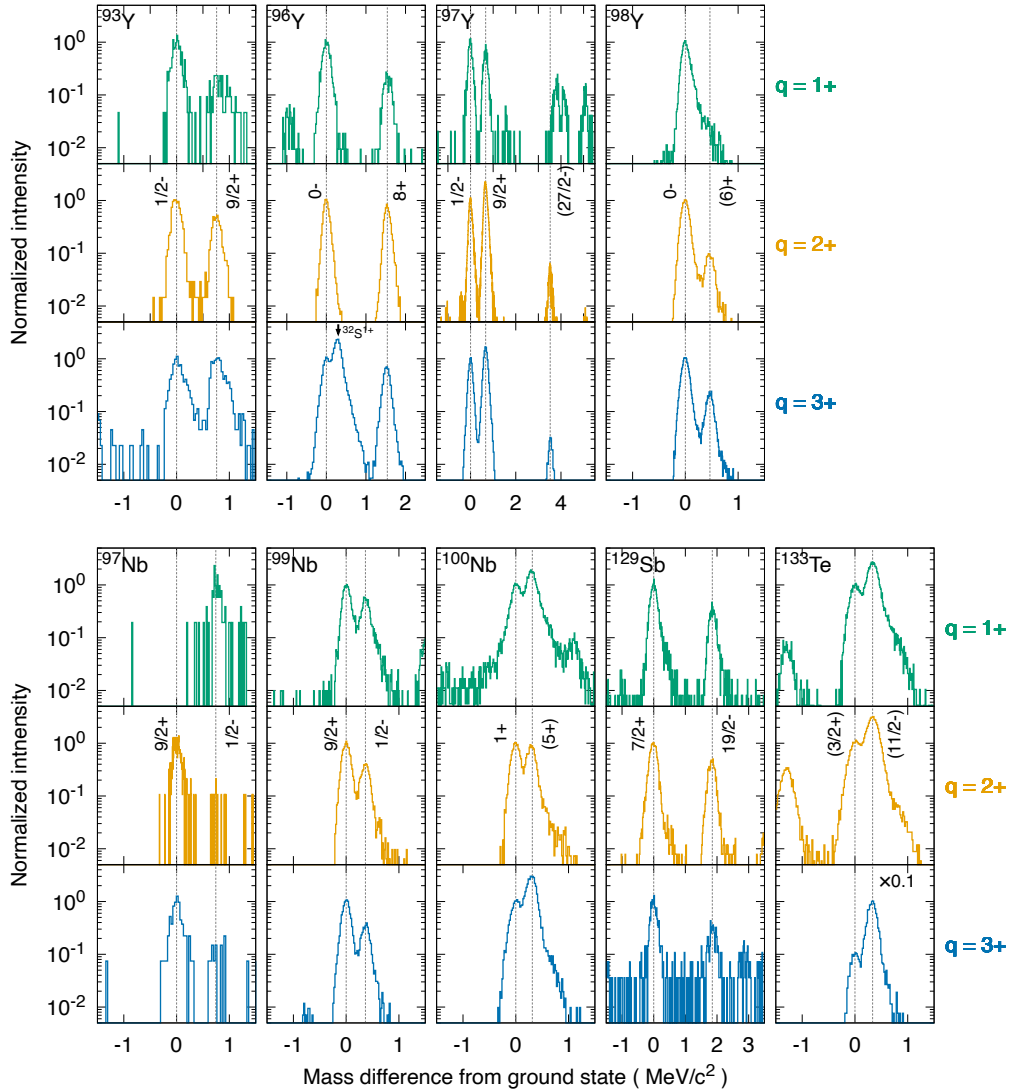


Figure 3: Time-of-flight spectra where the horizontal axis has been converted to the mass-energy relative to the ground state. Peak intensities are normalized to the ground state intensity of each nuclide. The dashed lines show the position of the ground and the isomeric states of interest; ^{97}Y has two isomeric states. Spin-parity of each state is also indicated with the dashed line; the parentheses denote prediction values.

performed similar measurements, measuring the relative yields across the 1+, 2+, and 3+ along isotopic chains for several elements that could be extracted from the CHeGC.

The measured isomeric yield ratios are plotted in the upper panel of Fig. 4, using the 3+ values for normalization to account for the initial isomeric yield ratio populated by the fission process. The spin difference between the ground and isomeric states ranges from $\Delta I = -4$ to $\Delta I = 13$ in the present measurements based on the spin values as evaluated in NUBASE2020 [8]. The yield ratios vary by four orders of magnitude, with a dependence on ΔI clearly visible, especially for the 1+. The ratios in the 2+ are distributed around unity with a weak spin difference dependence visible.

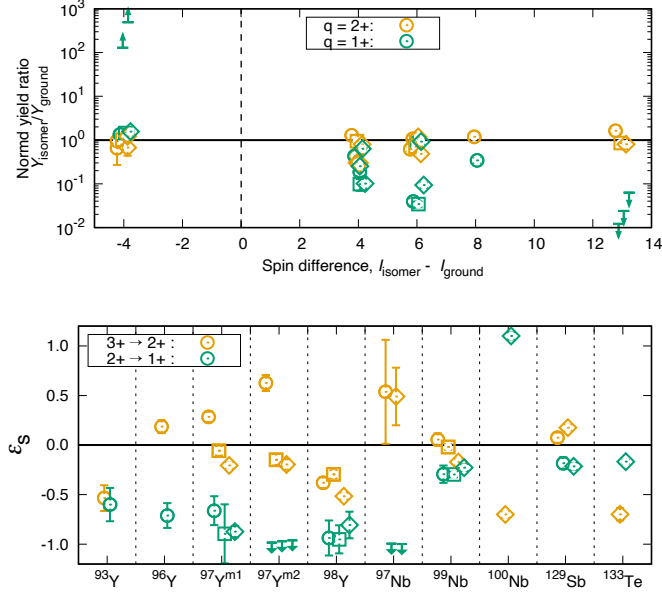


Figure 4: (Upper panel) Normalized yield ratios of the ground and isomeric state's peaks. All values are normalized by the values of the 3+ state. Several series of measurements were performed; the result of each is shown with a unique symbol shape. (Lower panel) Spin enrichment factor regarding the ground and isomeric states pair.

To quantify the change of the ion yield ratio associated with the charge state changing from q to q' , in an analogy to the isotope enrichment factor [1], we introduce a spin enrichment factor, ε_S , defined to be

$$\varepsilon_S(q, q') \equiv \frac{\rho(q')}{\rho(q)} - 1, \quad (1)$$

where ρ is an ion yield ratio between the higher- and lower-spin states, represented by

$$\rho(q) \equiv \frac{Y_{\text{High}}(q)}{Y_{\text{Low}}(q)}. \quad (2)$$

With this definition, a positive (negative) ε_S -value means that the higher (lower) spin component is concentrated along with the change in the charge state.

The lower panel of Fig. 4 plots the ground and isomeric state pairs' ε_S . The same measurements were performed several times for some nuclides, which are indicated with different symbols. We observe no case that both $\varepsilon_S(3+, 2+)$ (hereafter denoted as $\varepsilon_{S,32}$) and $\varepsilon_{S,21}$ are zero within 1σ , indicating that this ICSD anomaly is reproducible. The absolute values of ε_S are an order of 10^{-1} and are sufficiently large compared with the typical isotope enrichment factor (ranging from 10^{-4} to 10^{-3}) due to the MDE and the NFSE. No definitive correlation to a mass number is confirmed for the yttrium and

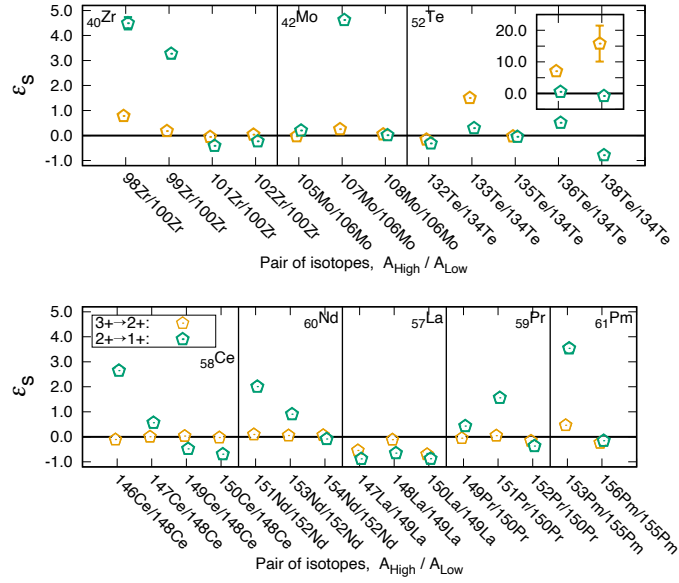


Figure 5: Spin enrichment factor regarding the pairs of isotopes. The horizontal axis shows the combinations of the isotopes. They are also given for convenience for the even- A – even- A pairs of the even atomic number elements. Other notations are the same as the lower panel of Fig. 4.

niobium isotopes. In addition, since the helium atoms have a dominant contribution in the ETs, the magnetic isotope effect could not work in the present condition. Thus, the observed ICSD does not match the known MDE and MIE features.

The CHeGC condition of each measurement series was slightly different; in the first series, the intensities of impurities were higher than all others, as shown by the 1+ TOF spectra in Fig. 2. The $\epsilon_{S,32}$ values of $^{79}\text{Y}^{m1,m2}$ at the first series (open circles in Fig. 4) seem to be outliers. In contrast, the ^{98}Y case shows consistent results in all three series. This implies that the sensitivity to the impurities in the filled helium gas can vary for different isotopes and nuclear states.

If the difference in the spin values of the ground and isomeric states causes an ICSD anomaly, non-zero ϵ_S should be observed for the pairs of isotopes for given elements with different ground state spins. The results for several such isotope pairs are plotted in Fig. 5, and most cases indeed show the non-zero ϵ_S values.

Zirconium's atomic number (Z) is forty, and the ground state spin of the even-even isotopes of zirconium is always zero. This means that the ϵ_S of any pair of even- A zirconium isotopes would be zero if they do not have long-lived nuclear isomeric states. Because there is no hyperfine interaction for zero-spin atomic nuclei, and the states of the electrons are the same in these even- A isotopes (the known MDE and MIE remain, but their magnitude is negligible in the present measurements). However, all ϵ_S of the

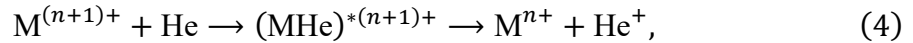
zirconium isotope pairs show non-zero values. The same situation is also confirmed in the other even- Z cases. We will revisit this point later in the following section.

Hereafter, we propose probable mechanisms that explain an ICSD anomaly. First, let us consider the case of the isomeric yield ratios. For most of the yttrium and niobium isotopes and the antimony isotopes, ε_S satisfies the magnitude relationship:

$$|\varepsilon_{S,21}| > |\varepsilon_{S,32}| \text{ and } \varepsilon_{S,21} < \varepsilon_{S,32}. \quad (3)$$

The first relation, $|\varepsilon_{S,21}| > |\varepsilon_{S,32}|$, would originate from the fact that the abundance of the 2+ state is dominant in the ICSD, while the 1+ state is a minor term. Because a small change in the yield ratio of the 2+ ions significantly impacts the yield ratio of the 1+ ions. The simplest supposition leading to the second relation, $\varepsilon_{S,21} < \varepsilon_{S,32}$, is that only the lower-spin components of 2+ ions go to the 1+: this process results in $\varepsilon_{S,21} < 0$ and $\varepsilon_{S,32} > 0$. However, the negative $\varepsilon_{S,32}$ -values are also observed in the lower panel of Fig. 4, which means the influx of the lower-spin components from the 3+ contributes. *Thus, the trend of Eq. 3 implies the existence of “relative” enhancement of the electron capture process of the lower-spin components, which is a major point from the observed ICSDs.*

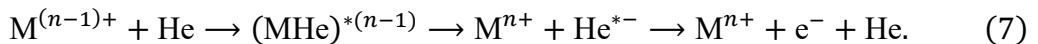
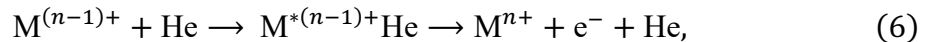
The ET under the condition where the charge-exchange equilibrium is frozen will be considered in the following. We start by setting two assumptions. The first one is that the collision of incoming ions always occurs against neutral helium atoms, meaning that a contribution from possible impurities is neglected. Such an assumption seems justified by the relative lack of observed radio-molecular ions. The second assumption is the low-energy limit; the kinetic energy of the incoming ion, M , is smaller than ~ 0.02 MeV/nucleon, where the relative velocity to a helium atom is slower than the Bohr velocity. In this condition, the collision time is sufficiently longer for a valence electron to go around the colliding atoms. Consequently, the electron capture reaction occurs via the forming of a quasi-molecular state (QMS)



only when the energy relation between their ionization potentials (IP s) and the external energy contribution (E_{exter}) satisfies the relation of

$$IP_{n+1}(M) + E_{\text{exter}} > IP_1(\text{He}) = 24.6\text{eV}. \quad (5)$$

In the inverse - the electron stripping reaction of the ions - two different processes can be considered:



For Eq. 6, an external energy contribution exceeding the $IP_n(M)$ is needed to occur. Forming a helium anion, He^{*-} , from ground-state helium requires an additional energy of 19.8 eV [9]. Thus, $IP_n(M)+19.8$ eV is the threshold of the process of Eq. 7. From the experimental results regarding the ion equilibrium charge state in helium gas [10], the

external energy contribution is insufficient to keep the charge-exchange equilibrium in the present low-energy condition. This indicates that once ICSD deviates from that of the equilibrium, it is difficult to return to it.

In the low-energy limit, the instantaneous ET described by the velocity matching between the helium's valence electron and the unoccupied orbits of the ions no longer occurs. Then, forming the QMS is crucial in the ET process. Nuclear spin could prevent the forming of the QMS if it significantly changes the effective potential or the configuration of the molecular orbits of the QMS, which is occupied by a transferring electron. This could suppress the ET processes described by Eqs. 4 and 7 for the higher-spin case, while the electron stripping process of Eq. 6 can still occur. In contrast, all three ET processes would be allowed in the lower-spin case. Consequently, the relative enhancement of the electron capture process of the lower-spin components would be established, and the ICSD differences would appear depending on nuclear spin.

Considering nuclear spin only, the non-zero ε_S in the even-even isotope pairs in Fig. 5 cannot be accounted for. In the zirconium case, the drop of ε_S -value can be found between $A = 99$ and $A = 101$. The result of the zirconium isotope laser spectroscopy measurement [11] shows a jump of charge radii at $A = 100$, meaning a nuclear shape transition exists. If deformed, non-spherical Coulomb potential caused by a highly deformed atomic nucleus could change the configuration of the QMS, the nuclear shape difference would be one of the possible origins of an ICSD anomaly. For the tellurium isotopes, the change of the charge radii trend is observed at $A = 135$ [12], and the smooth increase of the nuclear deformation is confirmed for the cerium isotopes of $A = 140$ to 148 [13]. These experimental results are consistent with the observed ε_S -value trends of both elements. This anomalously large NFSE coexists with the possible mechanism based on nuclear spin.

Finally, it is worth noting that one possible reason this anomaly had not been observed previously may be the low abundance—typically less than 10%, with few exceptions—of isotopes with a finite nuclear spin in the elements heavier than iron. Thus, investigating this phenomenon becomes challenging when only stable nuclides are considered.

We have discovered an ion charge state distribution anomaly, indicating that the state of the atomic nuclei significantly affects the electron transfer between helium atoms and the radioisotope ions having various nuclear states. The framework of the mass-dependent and mass-independent isotope effects cannot explain this anomaly, and the probable mechanisms of this phenomenon were discussed. This could be understood to arise from the change in the stability of the intermediate quasi-molecule state of the electron transfer caused by the difference in nuclear states. This should prompt a reconsideration of the nuclear effect on interatomic interactions, such as low-energy atomic collisions. Furthermore, this effect could provide new insights into isotopic chemistry.

References

1. J. Bigeleisen, M. G. Mayer, Calculation of Equilibrium Constants for Isotopic Exchange Reactions. *The Journal of Chemical Physics* **15** 261–267 (1947). doi: 10.1063/1.1746492
2. S. Yang, Y. Liu, Nuclear field shift effects on stable isotope fractionation: a review. *Acta Geochimica* **35**, 227–239 (2016). doi: 10.1007/s11631-016-0109-3
3. A. L. Buchachenko, Mass-Independent Isotope Effects. *The Journal of Physical Chemistry B* **117**, 2231–2238 (2013). doi: 10.1021/jp308727w
4. O. Vardi, N. Maroudas-Sklare, Y. Kolodnya, A. Volosniev, A. Saragovi, N. Galili, S. Ferrera, A. Ghazaryan, N. Yuran, H. P. Affek, B. Luz, Y. Goldsmith, N. Keren, S. Yochelis, I. Halevy, M. Lemeshko, and Y. Paltiel, Nuclear spin effects in biological processes. *Proceedings of the National Academy of Sciences* **120(32)**, e2300828120 (2023). doi: 10.1073/pnas.230082812
5. P. Schury, M. Wada, Y. Ito, F. Arai, S. Naimi, T. Sonoda, H. Wollnik, V. Shchepunov, C. Smorra, C. Yuan, A high-resolution multireflection time-of-flight mass spectrograph for precision mass measurements at RIKEN/SLOWRI. *Nuclear Instruments and Methods in Physics Research Section B* **335**, 39 – 53 (2014). doi: 10.1016/j.nimb.2014.05.016
6. S. Kimura, M. Wada, H. Haba, H. Ishiyama, S. Ishizawa, Y. Ito, T. Niwase, M. Rosenbusch, P. Schury, A. Takamine, Comprehensive mass measurement study of ²⁵²Cf fission fragments with MRTOF-MS and detailed study of masses of neutron-rich Ce isotopes. *Physical Review C* **110**, 045810 (2024). doi: 10.1103/PhysRevC.110.045810
7. M. Wada, Y. Ishida, T. Nakamura, Y. Yamazaki, T. Kambara, H. Ohyama, Y. Kanai, T.M. Kojima, Y. Nakai, N. Ohshima, A. Yoshida, T. Kubo, Y. Matsuo, Y. Fukuyama, K. Okada, T. Sonoda, S. Ohtani, K. Noda, H. Kawakami, I. Katayama, Slow RI-beams from projectile fragment separators. *Nuclear Instruments and Methods in Physics Research Section B* **204**, 570 – 581 (2003). doi: 10.1016/S0168-583X(02)02151-1
8. F. Kondev, M. Wang, W. Huang, S. Naimi, G. Audi, The NUBASE2020 evaluation of nuclear physics properties. *Chinese Physics C* **45**, 030001 (2021). doi: 10.1088/1674-1137/abddae
9. A. Mauracher, M. Daxner, J. Postler, S. E. Huber, S. Denifl, P. Scheier, J. P. Toennies, Detection of negative charge carriers in superfluid helium droplets: The metastable anions He*⁻ and He₂*⁻. *The Journal of Physical Chemistry Letters* **5**, 2444–2449 (2014). doi: 10.1021/jz500917z
10. K. E. Gregorich, Simulation of recoil trajectories in gas-filled magnetic separators, *Nuclear Instruments and Methods in Physics Research Section A* **711**, 47–59 (2013). doi: 10.1016/j.nima.2013.01.020

11. H. L. Thayer, J. Billowes, P. Campbell, P. Dendooven, K. T. Flanagan, D. H. Forest, J. A. R. Griffith, J. Huikari, A. Jokinen, R. Moore, A. Nieminen, G. Tungate, S. Zemlyanoi, and J. Äystö, Collinear laser spectroscopy of radioisotopes of zirconium, *Journal of Physics G* **29**, 2247–2262 (2003). doi: 10.1088/0954-3899/29/9/318
12. R. Sifi, F. Le Blanc, N. Barré, L. Cabaret, J. Crawford, M. Ducourtieux, S. Essabaa, J. Genevey, G. Huber, M. Kowalska, C. Lau, J. K. P. Lee, G. Le Scornet, J. Oms, J. Pinard, B. Roussière, J. Sauvage, M. Seliverstov, H. Stroke, and ISOLDE, Laser spectroscopy measurements of neutron-rich tellurium isotopes by COMPLIS. *Hyperfine Interact* **171**, 173–179 (2006). doi: 10.1007/978-3-540-71113-1_16
13. B. Cheal, M. Avgoulea, J. Billowes, P. Campbell, K. T. Flanagan, D. H. Forest, M. D. Gardner, J. Huikari, B. A. Marsh, A. Nieminen, H. L. Thayer, G. Tungate, and J. Äystö, Collinear laser spectroscopy of neutron-rich cerium isotopes near the $N = 88$ shape transition, *Journal of Physics G* **29**, 2479–2484 (2003). doi: 10.1088/0954-3899/29/11/003
14. Y. Ito, P. Schury, M. Wada, S. Naimi, T. Sonoda, H. Mita, F. Arai, A. Takamine, K. Okada, A. Ozawa, H. Wollnik, Single-reference high-precision mass measurement with a multireflection time-of-flight mass spectrograph. *Physical Review C* **88**, 011306 (2013). doi: 10.1103/PhysRevC.88.011306
15. K. Lan, J.W. Jorgenson, A hybrid of exponential and Gaussian functions as a simple model of asymmetric chromatographic peaks. *Journal of Chromatography A* **915(1-2)**, 1–13 (2001). doi: 10.1016/S0021-9673(01)00594-5

Acknowledgments: This study was supported by the Japan Society for the Promotion of Science KAKENHI, Grant Numbers 17H06090, 22H04946, 19K14750, and 23K13137.

Author Contributions: SK: Conceptualization, Formal analysis, Investigation, Visualization, and Writing - Original Draft; MW: Conceptualization, Supervision, and Funding acquisition; HH: Resources; HI: Project administration; TN: Resources; MR: Resources and Writing - Review & Editing; PS: Resources and Writing - Review & Editing.

Data and materials availability: All data are available in the supplementary materials.

METHODS

The peak identification was done by determining ion mass. The mass-determining way is similar to the previous works with the MRTOF-MS [5]. The measured TOF value for an ion, having mass m and charge q , which undergoes n laps in the MRTOF-MS device, can be represented by

$$t_{\text{obs}} = (a + b \cdot n)\sqrt{m/q} + t_0, \quad (8)$$

where a and b are constants related to the non-reflection flight path and the path between consecutive reflections, respectively, and t_0 represents an electronic delay between the TDC start signal and the ion's actual ejection from the flat trap. The single reference method [14], which needs only one reference mass, is adopted to determine the mass of analyte ions. In this method, m_X , the ionic mass of nuclide X, is given by

$$m_X = \rho_{\text{tof}}^2 m_{\text{ref}} = \left(\frac{t_X - t_0}{t_{\text{ref}} - t_0} \right)^2 m_{\text{ref}}, \quad (9)$$

where ρ_{tof} is the TOF ratio, t_X and t_{ref} are the TOF of nuclide X and the reference ion, respectively, m_{ref} is the mass of the reference ion, and t_0 is the constant time offset within the measurement system mentioned above.

A phenomenological fitting function, based on an exponential-Gaussian hybrid function [15], was used to fit non-Gaussian-shape peaks accurately. In the present study, we employed the function:

$$f(\tau) = \begin{cases} \left(\frac{\kappa}{\sigma}\right) \exp\left[\frac{t_{s1}(t_{s1} - 2\tau)}{2\sigma^2}\right] & (\text{for } \tau < t_{s1}) \\ \left(\frac{\kappa}{\sigma}\right) \exp\left[\frac{\tau^2}{2\sigma^2}\right] & (\text{for } t_{s1} \leq \tau < t_{s2}) \\ \left(\frac{\kappa}{\sigma}\right) \exp\left[\frac{t_{s2}(t_{s2} - 2\tau)}{2\sigma^2}\right] & (\text{for } \tau \geq t_{s2}) \end{cases} \quad (10)$$

where t_{si} denotes the range of each sub-function, the variable τ is defined as $\tau \equiv t - \mu$, where μ is the peak center used in the mass determinations.

Herein, we set a presumption about the peak shape: the peaks of the ions belonging to the same A/q series have an identical shape. Based on this assumption, the only free parameters for each peak in the fitting function are the peak center μ and the peak height κ for the species of interest. In the fitting algorithm, to improve the mass precision, the τ parameter was treated as a function of t , t_{ref} , and ρ_{tof} . Then, the fitting function F for N peaks was described by

$$F(t, t_{\text{ref}}, \rho_{\text{tof}1}, \dots, \rho_{\text{tof}N}, \kappa_1, \dots, \kappa_N) = \sum_{i=1}^N f(t, t_{\text{ref}}, \rho_{\text{tof}i}, \kappa_i, \sigma, t_{s1}, t_{s2}). \quad (11)$$

The ion yield ratios were determined using peak fit and event counting. The former was used for the ground and isomeric state pairs. In this case, the $\rho(q)$ can be represented by the peak height parameter κ as follows;

$$\rho(q) = \frac{\kappa_{\text{High}}}{\kappa_{\text{Low}}}. \quad (12)$$

Event counting was applied to the isotope pair measurements because the presumption regarding the peak shape is not always valid. An integrated region for event counting was determined by the peak fit to a single A/q series, and then they were calculated. In the ideal condition that two peaks are separated and their statistics are high enough, both methods must return the same value. For example, in the case of $^{96}\text{Y}^{2+}$, $\rho(2+) = 0.790(14)$ is obtained via the event counting and agrees on the value of the peak fit of 0.791(51).

SUPPLEMENTARY MATERIALS

Decay production

We will comment on decay production inside the CHeGC. The kinetic energy distribution of the fission fragments is wide for the “thin” CHeGC, and they should, for the most part, be stopped in the degrader on the fission sources or implanted in the materials inside the CHeGC. The implanted radioactive ions will decay, and some could recoil out from the material surfaces into the helium gas. In addition, the ions thermalized in the helium gas can also decay within a certain time and produce other nuclides. The ICSD produced via these decay productions should differ from that of the ET; thus, the measured ICSD must consist of at least two components having different origins. In most cases, the most significant change in the ion yield ratio occurs between 2+ and 1+, and this suggests the possibility of the contribution from the decay production being substantial to the yield ratios at 1+ and weak for 2+ and 3+. The following will discuss whether the decay production can explain the measured $\rho(1+)$ -values.

The mass measurement of the single charged $A = 98$ isobar series was performed, and the ^{98}Nb mass excess was determined to be $-83475(12)$ keV. This value is $49(14)$ keV heavier than the ground state’s literature value and is close to the center between the ground state and the isomeric state of $E_X = 84(4)$ keV and $T_{1/2} = 51.1(4)$ min. Thus, the fraction of the isomeric state is approximately half in the observed $^{98}\text{Nb}^{1+}$ peak. However, in the β^- -decay scheme of ^{98}Zr , the parent nuclide of ^{98}Nb , there is no branch to the isomeric state, and the parent state directly decays to the daughter’s ground state. From this, the contribution of the decay production in 1+ would be half of the total count at a maximum. For example, in the case of ^{97}Y , the measured $\rho(1+)$ regarding the first isomeric state ($m1$) was $0.292(15)$. The isomeric state branching ratio at the ^{97}Sr β^- -decay can be estimated at 20.8% based on the reported β^- -delayed γ -ray intensity. Assuming the decay production contribution is half, and the remaining half is the same as 3+, $\rho(3+) = 2.90(4)$ equivalent to the isomeric state fraction of 74.4%, one can get $\rho(1+) = 0.908$. This value is significantly different from the measured value, and then we conclude that the decay production does not resolve the observed ICSD.

Table I.

Information on the measurement conditions. A single helium cylinder was used for each series of measurements.

Meas. #	Date	252Cf source		Gas-cell temp.
		Serial #	Ref. date	
1	March 2023	S4-608	15 th March 2020	47.1 K
2	December 2023	S4-608	15 th March 2020	55.9 K
3	January 2024	W6-031	1 st December 2023	56.0 K
4	February 2024	W6-031	1 st December 2023	46.6 K

Table II.

The observed intensity ratio between ground and isomer states and the related nuclear properties. All values of I^π are taken from NUBASE2020, and the brackets indicate that the corresponding values are predicted ones.

Nuclide	I^π		Meas. #	ρ		
	Ground state	Isomeric state		1+	2+	3+
^{93}Y	1/2-	9/2+	1	0.199(30)	0.497(58)	1.07(12)
^{96}Y	0-	8+	1	0.229(27)	0.791(51)	0.667(19)
^{97}Y , m1	1/2-	9/2+	1	0.73(10)	2.16(11)	1.682(92)
			3	0.279(82)	2.66(12)	2.82(19)
			4	0.292(15)	2.302(67)	2.895(35)
^{97}Y , m2	1/2-	(27/2-)	1	0.0018 ^a	0.0462(30)	0.0284(22)
			3	0.0034 ^a	0.1212(68)	0.142(10)
			4	0.0017 ^a	0.1136(60)	0.1412(40)
^{98}Y	0-	(6 or 7)+	1	0.0108(18)	0.1698(83)	0.274(17)
			3	0.00674(93)	0.1383(51)	0.196(14)
			4	0.0199(26)	0.1027(28)	0.2119(60)
^{97}Nb	9/2+	1/2-	1	0.017 ^a	12.5(62)	8.2(25)
			4	0.065 ^a	12.4(34)	8.4(18)
^{99}Nb	9/2+	1/2-	1	1.93(17)	2.74(17)	2.59(18)
			3	2.080(54)	2.957(87)	3.02(17)
			4	1.930(63)	2.499(66)	3.016(79)
^{100}Nb	1+	(5+)	4	1.745(40)	0.830(20)	2.763(63)
^{129}Sb	7/2+	19/2-	1	0.333(20)	0.408(20)	0.379(63)
			4	0.339(12)	0.4306(98)	0.366(38)
^{133}Te	(3/2+)	(11/2-)	4	2.496(49)	2.996(31)	9.91(88)

^a Upper limit

Table III.

The observed intensity ratio between the isotopes with different mass numbers. All values of I^π are taken from NUBASE2020, and the brackets indicate that the corresponding values are predicted ones. Higher- and lower-spin states are defined for convenience for the even-A- even-A pairs of the even atomic number elements.

Element	Lower spin		Higher spin		Meas. #	ρ		
	A	I^π	A	I^π		1+	2+	3+
Even atomic number								
Zr	100	0+	98	0+	2	2.53(12)	0.460(13)	0.258(20)
	100	0+	99	1/2+	2	2.797(77)	0.655(14)	0.5547(94)
	100	0+	101	3/2+	2	0.471(24)	0.797(12)	0.843(13)
	100	0+	102	0+	2	0.536(21)	0.695(15)	0.671(11)
Mo	106	0+	105	(5/2-)	2	1.231(20)	1.0248(65)	1.056(14)
	106	0+	107	(1/2+)	2	2.547(37)	0.4530(37)	0.3614(63)
	106	0+	108	0+	2	0.2030(60)	0.1997(46)	0.1910(91)
Te	134	0+	132	0+	2	0.3004(33)	0.439(18)	0.522(31)
	134	0+	133	(3/2+),(11/2-)	2	0.7749(92) ^a	0.596(17) ^a	0.2388(41) ^a
	134	0+	135	(7/2-)	2	0.5903(76)	0.620(18)	0.641(17)
	134	0+	136	0+	2	0.3745(56)	0.2484(99)	0.0307(14)
	134	0+	138	0+	2	0.0346(10)	0.159(10)	0.0095(34)
Ce	148	0+	146	0+	2	1.820(41)	0.499(14)	0.560(13)
	148	0+	147	(5/2-)	2	1.139(23)	0.728(12)	0.7240(83)
	148	0+	149	(3/2-)	2	0.415(11)	0.798(11)	0.7746(87)
	148	0+	150	0+	2	0.1708(64)	0.5615(99)	0.5784(71)
Nd	152	0+	151	3/2+	2	1.466(49)	0.488(11)	0.445(19)
	152	0+	153	(3/2-)	2	1.93(11)	1.016(22)	0.963(34)
	152	0+	154	0+	2	0.876(34)	0.961(18)	0.904(31)
Odd atomic number								
La	149	(3/2-)	147	(5/2+)	2	0.314(14)	2.653(84)	5.828(96)
	149	(3/2-)	148	(2-)	2	0.736(25)	2.099(58)	2.361(43)
	149	(3/2-)	150	(3+)	2	0.0106(23)	0.0831(81)	0.2740(90)
Pr	150	1-	149	(5/2+)	2	1.148(27)	0.8023(78)	0.847(23)
	150	1-	151	(3/2-)	2	2.785(57)	1.090(14)	1.041(27)
	150	1-	152	4+	2	0.427(14)	0.6774(69)	0.807(22)
Pm	155	(5/2-)	153	5/2-	2	1.687(67)	0.3716(63)	0.254(24)
	155	(5/2-)	156	4+,(1+)	2	0.707(35) ^a	0.834(11) ^a	1.102(64) ^a

^a The ratio to the sum of the ground and isomeric states